9th Asia-Pacific Conference on Wind Engineering
Auckland, New Zealand
3-7 December 2017

Wind pressures and flow fields around large-span roofs with various shapes

Y. Takadate[1] and Y. Uematsu[1]

[1]Department of Architecture and Building Science
Tohoku University, Sendai, Miyagi, 980-8579, Japan

Abstract

The present paper discusses the characteristics of the flow around and the wind pressures on large-span roofs with various shapes based on a computational fluid dynamics (CFD) with large eddy simulation (LES). Focus is on the effects of the roof shape and the turbulence of approach flow on these characteristics. Three kinds of roofs, i.e. flat, cylindrical and suspended roofs are investigated in two kinds of approach flows, i.e. a smooth uniform flow and a turbulent boundary layer simulating open country exposure. The turbulent boundary layer is generated by a preliminary analysis that simulates a wind tunnel flow developing on the floor with roughness blocks and spires. The simulation method of the flow around the building model is verified by a comparison of the results with the previous experimental results with flat roof models. The results of a series of numerical simulation indicate that the pressures and flow fields are significantly affected by the roof curvature as well as by the flow turbulence. It is also found that the pressure field on the roof has a convective nature in any roof case. The convection velocity depends on the roof shape as well as the turbulence of approach flow.

Introduction

In recent years, many large-span structures, such as stadiums, auditoriums and airport terminals, have been constructed all over the world. Membranes are often used for these structures. Because these roofs are inherently light and flexible, they are vulnerable to dynamic wind actions. In some cases, aerodynamically unstable oscillations, such as a flutter, may be induced.

Many researchers have investigated the wind loads, wind-induced oscillations and aerodynamic stability of large-span roofs with various shapes. Uematsu and Uchiyama [9] investigated the wind-induced dynamic behavior of one-way type suspended roofs in a smooth flow. They showed that large-amplitude oscillation was induced at a critical wind speed due to structural and/or aerodynamic instability, which was related to the mass and initial tension introduced into the roof. Furthermore, they implied that the convective nature of pressure fluctuations on the roof played an important role in the dynamic behavior and the aerodynamic stability of the first asymmetric mode. Matsumoto [3, 4] also investigated the aerodynamic stability of such roofs in a wind tunnel. He showed that the unstable oscillation was related to the shedding of vortices generated by the flow separation at the leading edge. He proposed a mechanism of unstable oscillations based on the relation between the vortex behavior and roof oscillation. Ueda et al. [7, 8] made a detailed measurement of wind pressures on flat roofs in a turbulent boundary layer. They investigated the effects of span/height ratio on the pressure distribution. Ohkuma et al. [5] investigated the aerodynamic stability of a flat roof in a wind tunnel using a forced-vibration technique. They measured the unsteady aerodynamic forces, represented by the aerodynamic stiffness and damping, acting on an oscillating roof in the first asymmetric mode. They proposed an analytical method for evaluating the dynamic response considering the flow-structure interaction (FSI). Using a similar technique, Ding et al. [2] discussed the characteristics of unsteady aerodynamic forces on cylindrical roofs based on a wind tunnel experiment as well as on a CFD simulation using LES. The CFD simulation could provide the results for a wider range of reduced wind speed than the wind tunnel experiment. These previous studies indicate that the wind loads and aerodynamic stability are strongly dependent on the flow turbulence and roof shape. However, no systematic studies have been made on this subject.

Recently, both computer technology and CFD technique have been developed remarkably, which enables us to investigate the FSI of flexible structures in more detail. Furthermore, flow visualization by CFD is fairly useful for understanding the phenomenon.

In the present study, therefore, a CFD simulation with LES is applied to the flow around large-span roofs with various shapes, i.e. flat, cylindrical and suspended roofs. The final target of our study is to make clear the FSI effect on the dynamic behavior and aerodynamic stability of these roofs. As the first step of the study, the fundamental characteristics of the flow around these roofs and the resulting wind pressure distributions on them are investigated in the present paper. The analysis is limited to two-dimensional rigid models. First, the numerical simulation model including the inflow turbulence is verified by comparing the results with the previous experimental results. Then, the wind pressures on the roofs and the flow around the buildings are investigated based on the CFD simulation, focusing on the effects of flow turbulence and roof shape on the time-space correlations of the roof pressures.

CFD Simulation

Model Buildings

Three kinds of roof shapes, i.e. flat, cylindrical and suspended roofs, shown in figure 1 and table 1, are used in the present study. The values of rise/span ratio (h/L) in the cylindrical roof case and sag/span ratio (s/L) in the suspended roof case, and the span/eaves-height ratio (L/H) are determined based on a survey of practical large-span structures constructed in Japan. The span L and the eaves height H are assumed 120 m and 20 or 40 m, respectively. In the CFD simulation, the geometric scale is assumed 1/400, which corresponds to that of usual wind tunnel experiments. Note that these models are rigid and two-dimensional. No deformation and oscillation of the roof are considered in the present analysis.

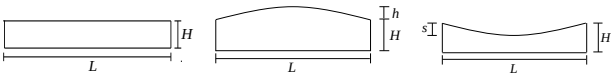

(a) flat roof (b) cylindrical roof (c) suspended roof

Figure 1. Shapes of large-span roofs under consideration.

Computational conditions

The flow simulation is performed by OpenFOAM (ver.2.3.1), an open source CFD code based on a finite-volume method (FVM), in which the large eddy simulation (LES) is used. The governing

	Rise/span (h/L) or sag/span(s/L) ratio	Length-height ratio (L/H)
Flat roof	0	3, 6
Cylindrical roof	0.1, 0.2	3, 6
Suspended roof	0.05, 0.1	3, 6

Table 1. Geometry of model buildings.

equations are a continuity equation and three-dimensional Navier–Stokes equations, represented by

$$\frac{\partial \bar{u}_i}{\partial x_i} = 0 \tag{1}$$

$$\frac{\partial \bar{u}_i}{\partial t} + \bar{u}_j \frac{\partial \bar{u}_i}{\partial x_j} = -\frac{1}{\rho}\frac{\partial \bar{p}}{\partial x_i} + \frac{\partial}{\partial x_j}\left(\nu \frac{\partial \bar{u}_i}{\partial x_j}\right) - \frac{\partial \tau_{ij}}{\partial x_j} \tag{2}$$

where symbols with overbar represent the grid-filtered values; x_i represents the coordinate; u_i is the velocity component in the x_i direction; p is pressure; and τ_{ij} is the sub-grid stress given by the Smagorinsky model [6] as follows:

$$\tau_{ij} = -2C_S \overline{\Delta}^2 \left|\bar{S}\right| \bar{S}_{ij} \tag{3}$$

$$\left|\bar{S}\right| = \sqrt{2\bar{S}_{ij}\bar{S}_{ij}}, \qquad S_{ij} = \frac{1}{2}\left(\frac{\partial \bar{u}_i}{\partial x_j} + \frac{\partial \bar{u}_j}{\partial x_i}\right) \tag{4), (5}$$

The standard Smagorinsky model with Van–Driest type wall damping function is employed for solving the sub-grid scale fluid motions. The model coefficient C_s is set to 0.12 [2]. Furthermore, pressure-implicit with splitting of operations (PISO) method is used for solving the pressure and velocity. The computational conditions are summarized in Table 2.

Inlet boundary	Smooth uniform flow and turbulent flow generated by a preliminary computation
Side and upper boundary	Free-slip
Floor and model boundary	No-slip
Outlet boundary	Free outflow
Convection scheme	Second-order central difference scheme
Time differential scheme	Second-order backward difference scheme
Numerical algorithm	PISO algorithm
Time Step	2.0×10^{-4} sec

Table 2. Computational conditions.

Inflow Turbulence Generation

A preliminary analysis corresponding to a wind tunnel experiment is made to generate the inflow turbulence. The computational domain is 3.0 m wide, 2.0 m high and 20 m long, which is divided into 4 blocks in the vertical direction with layer mesh, as shown in figure 2. Spires are installed at the beginning of the domain and many roughness blocks are distributed on the floor. Smooth uniform flow is given to the inlet boundary and the generated turbulent flow at the outlet boundary is used for the following analysis of the flow around a large-span roof structure. The number of mesh is approximately 4,200,000.

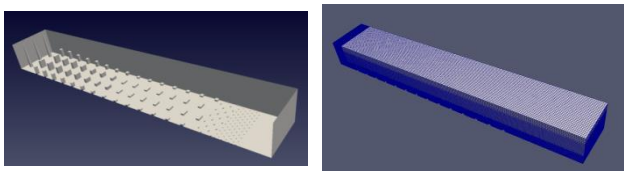

(a) Roughness arrangement (b) Grid division

Figure 2. Computational domain for generating inflow turbulence.

Figure 3(a) shows the mean velocity and turbulence intensity profiles obtained at the outlet plane. The solid lines represent the specifications of *the AIJ Recommendations for Loads on Buildings* [1]. It is found that the CFD results and the AIJ specifications agree well with each other. The power spectrum of velocity fluctuations in the stream-wise direction is shown in figure 3(b), where n and L_x represent the frequency and the longitudinal turbulence scale, respectively. The solid line represents the Karman-type spectrum. Due to a filtering effect, the values of power spectrum obtained from the CFD simulation are smaller than those of the Karman-type spectrum in a non-dimensional frequency range of $nL_x/U > 0.5$. However, these spectra agree well with each other in the smaller reduced frequency range, which more important for discussing the wind pressures on buildings. Hence, this turbulent boundary layer is used as the inflow for the following simulations.

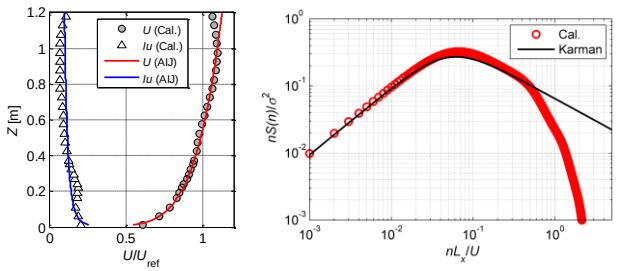

(a) Mean velocity and turbulence intensity (b) Power spectrum of fluctuating wind velocity

Figure 3. Velocity profiles and power spectrum.

Simulation method for the roofs with various shapes

Figure 4 shows the computational domain and mesh division for a flat roof with $L/H = 3$. The domain size is $12L(x) \times 2L(y) \times 4L(z)$. A base mesh is 0.05 m cube. The mesh is nested to concentrate the mesh near the surface of the building. The number of cells is approximately 1,500,000. The free-slip boundary condition is applied to the top and side walls, and the Spaliding wall function is applied to the floor and building walls. The wind pressures on the model surface are normalized to the wind pressure coefficients C_p by the mean velocity pressure q_H at the eaves height H. The wind pressures and wind speeds are sampled at a rate of 1000 Hz for 8 seconds, which corresponds to 10 minutes in full scale. The same computations are made five times, and the statistical values of wind velocities and pressures are evaluated by applying an ensemble average to the results of the 5 consecutive runs.

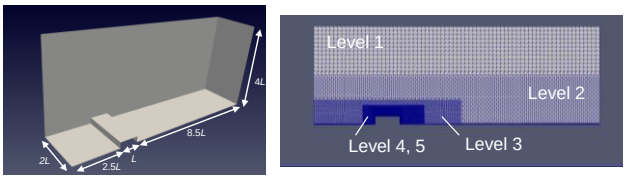

(a) Computational domain (b) Grid division

Figure 4. Simulation model for a flat roof with $L/H = 3$.

Pressure distribution around various kinds of roofs

Wind pressures on the flat roofs

Figure 5 shows the distributions of the mean and RMS fluctuating pressure coefficients, C_{p_mean} and C_p', along the centerline of the roof in the smooth and turbulent flows, in which x represents the distance from the leading edge. In these figures, the previous experimental results obtained by Ueda et al. [7, 8] are also plotted for a comparative purpose. The characteristics of the approach flows used in Ueda et al. [7, 8] and in the present simulations are summarized in table 3. The results of the CFD simulation are in good agreement with the experimental results. Although the distribution is strongly dependent on the flow turbulence, it is characterized by x/H despite the L/H ratio in both flows.

In the smooth flow, relatively large suctions are induced over a wider area, although the magnitude is not so large. The maximum value of C_p' occurs at $x/H = 3$–4. In the turbulent flow, on the other hand, larger suctions are induced in a small area near the leading

edge, i.e. $x/H < 2$. In this area, the pressure gradient is rather large. The maximum value of C_p' occurs at $x/H \approx 0$ and the distribution of C_p' is similar to that of C_p. Judging from the distributions of C_{p_mean} and C_p', the time-averaged reattachment point of the separated flow is located at $x/H \approx 4$ in the smooth flow, while at $x/H \approx 2$ in the turbulent flow. It is found that the characteristics of the flow around and the wind pressures on the roof are affected by the turbulence of approach flow, significantly.

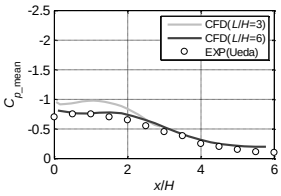

(a) Mean pressure coefficients (smooth flow)

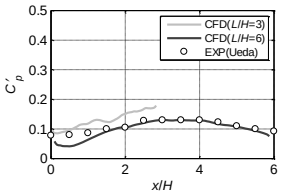

(b) RMS fluctuating pressure coefficients (smooth flow)

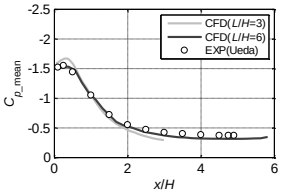

(c) Mean pressure coefficients (turbulent flow)

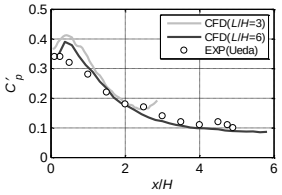

(d) RMS fluctuating pressure coefficients (turbulent flow)

Figure 5. Distributions of C_{p_mean} and C_p' on the flat roofs.

		α	I_{uH} (H=50 mm)	I_{uH} (H=100 mm)
Smooth flow	CFD	-	0%	0%
	EXP(Ueda)	-	0.5%	0.5%
Turbulent flow	CFD	0.15	18.7%	17.6%
	EXP(Ueda)	0.16	14.8%	12.7%

Table 3. Characteristics of the approach flows.

Wind pressures on cylindrical and suspended roofs

The distributions of C_{p_mean} and C_p' along the centerline of the cylindrical and suspended roofs in the smooth and turbulent flows are shown in figures 6 and 7, respectively. The abscissa of the figures is the distance S from the leading edge along the centerline of the roof, normalized by the total length S_{max}.

In the cylindrical roof case, the distribution of C_{p_mean} is strongly dependent on the rise/span ratio (r/L) as well as on the flow turbulence I_{uH}. The effect of r/L seems larger than that of I_{uH}. When $r/L = 0.1$, the flow separates at the leading edge and then reattaches soon at a point on the roof. As the L/H ratio and/or the I_{uH} values increase, the location of the reattachment point shifts windward, that is, the size of separation bubble decreases. When $r/L = 0.2$, such a separation bubble disappears. This feature means that the wind flows along the roof without separation. Large suctions are induced near the leading edge when $r/L = 0.1$, while near the rooftop when $r/L = 0.2$. The C_{p_mean} and C_p' distributions correspond well to each other, particularly in turbulent flow.

In the suspended roof case, the C_{p_mean} and C_p' distributions strongly dependent on the approach flow. Compared with the flat roof case, the roof is subjected to larger suctions in a wider area. This feature may be related to the behavior of the separated flow from the leading edge. The reattachment point is located at a more leeward point, particularly in the smooth flow. The distributions seems less sensitive to the s/L ratio.

Flow field around the structure

Figure 8 shows the distributions of mean wind velocity above a flat roof with $L/H = 6$, which is represented by the vectors. The flow separates at the leading edge ($x/H = 0$) and reattached at $x/H = 4$–5 in the smooth flow and at $x/H \approx 2$ in the turbulent flow as

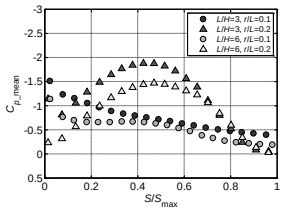

(a) Mean wind pressure coefficients (cylindrical roof)

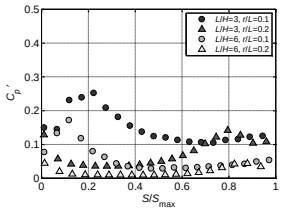

(b) RMS fluctuating pressure coefficients (cylindrical roof)

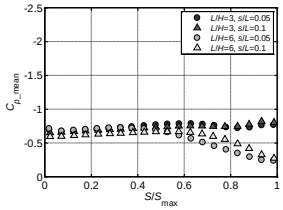

(c) Mean wind pressure coefficients (suspended roof)

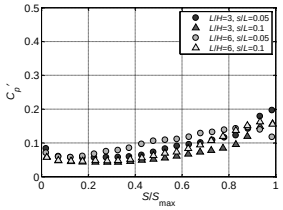

(d) RMS fluctuating pressure coefficients (suspended roof)

Figure 6. Distributions of C_{p_mean} and C_p' in smooth flow.

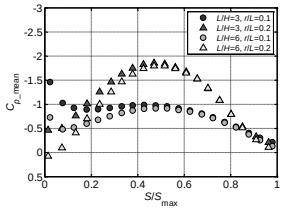

(a) Mean wind pressure coefficients (cylindrical roof)

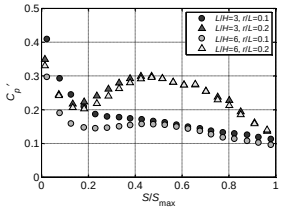

(b) RMS fluctuating pressure coefficients (cylindrical roof)

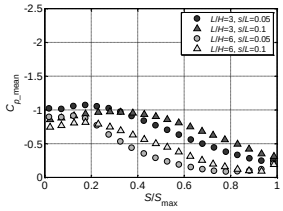

(c) Mean wind pressure coefficients (suspended roof)

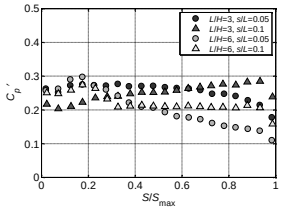

(d) RMS fluctuating pressure coefficients (suspended roof)

Figure 7. Distributions of C_{p_mean} and C_p' in turbulent flow.

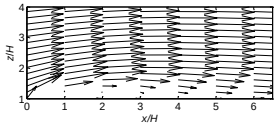

(a) Smooth flow

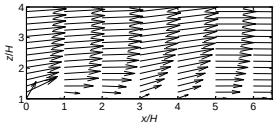

(b) Turbulent flow

Figure 8. Mean wind flow around the flat roof ($L/H = 6$).

expected from the distribution of C_{p_mean} shown in figure 5. A reverse flow can be seen near the roof in a windward area. The curvature of the separated flow is larger in the turbulent flow than in the smooth flow, generating a smaller separation bubble and a faster recovery of pressures on the roof. This feature indicates that the behavior of the separated flow from the leading edge is significantly affected by the turbulence of approach flow.

Figures 9–12 show the variations of the instantaneous distributions of wind velocities with time for the three kinds of roofs with $L/H = 6$. A comparison between figures 9 and 10 shows the effect of flow turbulence on the flow field around the flat roof. In the smooth flow case, the flow field is relatively steady, that is, the wind velocities above the roof change only slightly with time. In the turbulent flow case, on the other hand, the separated flow reattaches on the roof near the leading edge and the vorticities move to the leeward side with time. This result implies that the large vortices are difficult to be generated in the turbulent flow. In the case of cylindrical roof with $r/L = 0.1$ (figure 11), the flow separation is not clearly observed and the wind flows smoothly along the roof, compared with the flat roof. It is thought that the

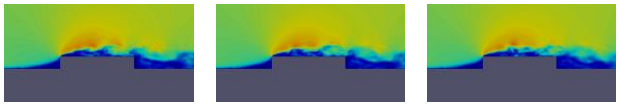

(a) t = 15.22 sec (b) t = 15.23 sec (c) t = 15.24 sec

Figure 9. Instantaneous distribution of wind velocity for the flat roof in smooth flow (L/H = 6).

(a) t = 15.6 sec (b) t = 15.61 sec (c) t = 15.62 sec

Figure 10. Instantaneous distribution of wind velocity for the flat roof in turbulent flow (L/H = 6).

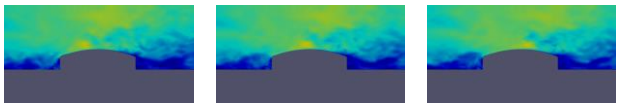

(a) t = 15.8 sec (b) t = 15.81 sec (c) t = 15.82 sec

Figure 11. Instantaneous distribution of wind velocity for the cylindrical roof in turbulent flow (L/H = 6, r/L = 0.10).

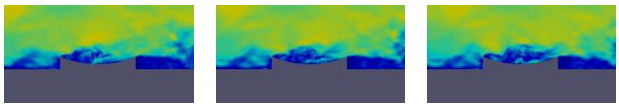

(a) t = 15.5 sec (b) t = 15.51 sec (c) t = 15. 52 sec

Figure 12. Instantaneous distribution of wind velocity for the suspended roof in turbulent flow (L/H = 6, s/L = 0.10).

large suctions near the rooftop are induced by the flow acceleration. Finally, in the case of suspended roof with s/L = 0.1 (figure 12), the flow separates at the leading edge and reattached at a point near the bottom of the roof. Relatively large separation bubble is generated.

Phase of pressure fluctuation on the roof

Time-space correlation of pressure fluctuations on the roof is discussed here, focusing on the phase differences between pressure fluctuations obtained at different points shown in figure 13. Figure 14 shows the phase angles of pressure fluctuations at two adjacent points. The abscissa is the reduced frequency defined by $n\Delta/U_H$, with n, Δ and U_H being frequency, distance between the two points and mean wind velocity at the eaves height, respectively. In any case, the phase angle is roughly proportional to the reduced frequency, although there is a scatter in the results. The convection velocity may be estimated by the following equation:

$$U_c = 2\pi n\Delta / \Theta_{i,j} \tag{6}$$

where U_c is the convection velocity of the roof pressures and $\Theta_{i,j}$ represents the phase angle. The value of U_c is approximately (0.5–0.6)U_H for the flat roofs (figure 14(a), (b)). The velocity for uniform flow is slightly slower than that for turbulent flow. However, these values agree well with those obtained by Ohkuma et al. [5] and Ueda et al. [8]. The value of U_c for the cylindrical roofs is approximately 0.8U_H (figure 14(c)), which is much larger than that for the flat roof. The value of U_c for the suspended roof is nearly equal to that for flat roof in a range of $n\Delta/U_H$ < 0.25 (figure 14(d)). These results suggest that the convection velocity of pressure fluctuations is closely related to the separated flow at the leading edge.

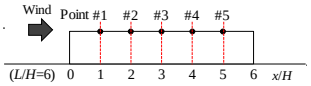

Figure 13. Sampling points of the wind pressures for computing the phase angles.

Concluding Remarks

Wind pressures on and flow around three kinds of large-span roofs were investigated based on the CFD simulation. The wind pressure distribution on the flat roof was in good agreement with the previous experimental data. Pressure distributions on and flow around the roofs were investigated in detail. Then, the time-space correlation of pressure fluctuations on the various roofs was made clear. Detail LES analysis, such as forced vibration analysis and the FSI analysis, for flexible models are planned in future study.

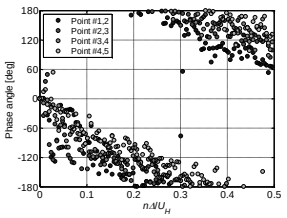

(a) Flat roof (L/H = 6, Smooth flow)

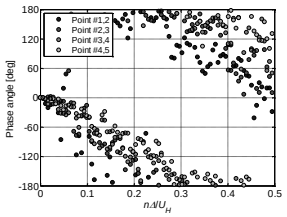

(b) Flat roof (L/H = 6, Turbulent flow)

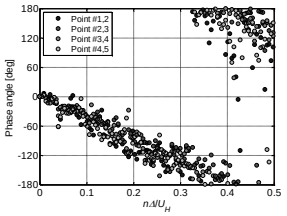

(c) Cylindrical roof (L/H = 6, r/L = 0.1, Turbulent flow)

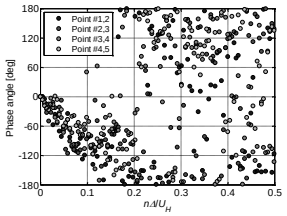

(d) Suspended roof (L/H = 6, s/L = 0.1, Turbulent flow)

Figure 14. Phase of pressure fluctuations at adjacent points for flat roof.

Acknowledgement

This work was supported by Grant-in-Aid for JSPS Fellows (Grant Number 16J01789).

References

[1] Architectural Institute of Japan, 2015. Recommendations for Loads on Buildings. Architectural Institute of Japan (in Japanese).

[2] Ding W., Uematsu Y., Nakamura M. & Tanaka S., Unsteady aerodynamic forces on a vibrating long-span curved roof, Wind and Structures, An Int'l Journal, 19(6), 2014, 649–663.

[3] Matsumoto T., On the mechanism of a self-excited oscillation of single curvature cable roofs, Journal of Wind Engineering, 36, 1988, 45–48 (in Japanese).

[4] Matsumoto T., On self-excited oscillation of the cable trussed roof with single curvature, Journal of Wind Engineering and Industrial Aerodynamics, 33, 1990, 131–138.

[5] Ohkuma T. & Marukawa H., Mechanism of aeroelastically unstable vibration of large span roof, Journal of Wind engineering, 42, 1990, 35–42 (in Japanese).

[6] Smagorinsky J., General circulation experiments with the primitive equations, Part I. The basic experiment. Monthly Weather Review, 91(3), 1963, 99–164.

[7] Ueda H., Tamura Y. & Fuji K., Effects of turbulence of approaching wind on mean wind pressures acting on flat roofs —Study on characteristics of wind pressures acting on flat roofs Part 1—, Journal of Structural and construction engineering, 425, 1991, 91–99 (in Japanese).

[8] Ueda H., Tamura Y., Fuji K. & Katsumura A., Effects of turbulence of approaching wind on fluctuating pressures acting on flat roofs —Study on characteristics of wind pressures acting on flat roofs Part 2—, Journal of Structural and construction engineering, 447, 1993, 17–30 (in Japanese).

[9] Uematsu Y. & Uchiyama K., Wind-induced dynamic behavior of suspended roofs, The Technology Reports of the Tohoku University, 47, 1982, 246–261.